Monocular Ranging for Small Unmanned Aerial Systems in the Far-Field

Chester V. Dolph,[1]
NASA Langley Research Center, Hampton, VA, 23681, USA

Cyrus Minwalla[2]
Scoped Systems, Ottawa, ON, K2G 7A5, Canada

Louis J. Glaab[3], B. Danette Allen[4]
NASA Langley Research Center, Hampton, VA, 23681, USA

and
Khan M. Iftekharuddin[5]
Old Dominion University, Norfolk, VA, 23529, USA

Recent proliferation of small Unmanned Aerial Systems (sUAS) applications requires onboard collision avoidance systems to mitigate the risk of collision with non-cooperative aircraft and manned aircraft, which may not see sUAS in time to perform an avoidance maneuver. An attractive avenue for onboard collision avoidance is the utilization of machine vision cameras due to their low size, weight and power (SWaP) requirements. In this paper, we characterize the range performance of a machine vision system developed in-house and mounted onto an sUAS. The technique was designed to estimate the performance of a sense-and-avoid system to ensure that the sensing components meet the well-clear requirements for the chosen platform and avoidance strategy. Experimental flight-test data was acquired from test-flights flown along multiple collision geometries for two intruders: a general Aviation (GA) aircraft and a fixed-wing sUAS. The ownship and both intruders were instrumented with inertial navigation systems (INS) recording position and attitude information. The range at first detection, R_0, was extracted from in-flight imagery of head-on collision course geometry synchronized with INS data from both aircraft and ground-truth values extracted from the raw imagery. This initial detection distance, R_0, scales with atmospheric attenuation. Therefore, under clear sky conditions, the derived R_0 value represents the upper bound on the detection range achievable by the test configuration of the detector. Results indicate that the maximum initial detection distance for a 4k resolution action camera fitted with a 41° Field of View (FOV) lens is 2.763 ± 0.037 km for a GA aircraft and 0.881 ± 0.061 km for a fixed-wing sUAS, respectively. The in results this study suggest that a vision-based detect and track system may be analyzed using the sensor characterization and contextualized within aircraft well-clear volumes.

Nomenclature

CNR	=	*Contrast to Noise Ratio*
FOV	=	*Field of View*
GA	=	*General Aviation*
GT	=	*Ground Truth*
I	=	*Intensity*
INS	=	*Inertial Navigation System*
MOPS	=	*Minimum Operational Performance Standards*
R	=	*Range*

---

[1] Aerospace Engineer, Aeronautics Systems Engineering Branch, AIAA Member.
[2] Principal, Scoped Systems.
[3] Aerospace Engineer, Aeronautics Systems Engineering Branch.
[4] NASA Senior Technologist (ST) for Intelligent Flight Systems, MS 233, AIAA Associate Fellow.
[5] Associate Dean for Graduate Research and Graduate Programs, Batten College of Engineering & Technology.

ROI = *Region of Interest*
sUAS = *small Unmanned Aerial System*
S_{th} = *Signal Threshold*

I. Introduction

The sUAS have numerous civil, scientific and commercial applications along with a hobby following in the private sector [1]. The sUAS are an enabling technology that allows for inspection of remote and hard to reach locations, such as rugged terrain or rural search and rescue operations. Package delivery is an example of a commercial application. The sUAS applications can present a challenge to safe operations of GA aircraft due to the exponential growth of consumer-grade camera-equipped sUAS capable of being flown without pilot intervention. Vision systems installed on sUAS vehicles can be used for onboard collision avoidance of other aircraft and the ability to determine the separation distance of the intruder aircraft is essential for effective avoidance maneuvers.

Extracting depth from a monocular camera is challenging because local image data may not be adequate for estimating depth at a location [2], however, contrast has been correlated to aircraft separation distance in [3]. This work performs a depth characterization of fixed-wing GA and fixed-wing sUAS using flight video recorded onboard sUAS for the detect and track pipeline described in [4]. The results of this work will be compared to the GA fixed-wing vs. helicopter ownship results discussed in [3]. This paper is organized with the following sections: background, range performance model, experimental methodology, analysis and results, and conclusion.

II. Background

This section presents a background on vehicle ranging and the status of sUAS Minimum Operation Performance Standards (MOPS) for onboard avoidance. Stereo vision is a well-researched technique that can be applied in multiple scenarios. It has been shown to reliably measure the distance between two cars [5] and for visual odometry from an autonomous vehicle [6]. However, stereo vision relies on depth from disparity, where a pixel difference between two targets is used to compute range. Therefore, stereo is only effective if the baseline distance between the two cameras is a reasonable proportion of the range to the target. For distant targets, such as aircraft on a collision course scenario, the baseline distance is much smaller relative to the target depth, forcing the disparity to within a single pixel, which cannot be disambiguated. Given the finite size of sUAS and collision sensing modalities constrained to machine vision systems, stereo vision is limited to detecting targets at 1 km or less or applied to the domain of obstacle avoidance. Furthermore, the use of stereo requires dedicating two or more sensors to the same scan region, as such doubling the size, weight and power requirements (SWaP) of the system. Therefore, monocular camera ranging is an attractive solution for depth estimation for an electro-optical sense and avoid system.

Monocular ranging from aircraft is a nascent field and thus this work also reviews ground-based car ranging. Monocular ranging may be used to measure the distance between two cars on the road as described in [7] and [8]. The work in [7] uses a priori knowledge of the fixed size of the license plate dimension and pinhole camera model to determine the range of the camera. Testing was performed for separation distances between 1 to 7 meters. The error between the ground-truth measurement and monocular estimate ranged from 1 to 10% error. The authors perform a real-time test but do not report accuracy for the real-time test.

The work in [8] describe three ways of measuring the distance: static image, static image model, and space geometry. The static image technique uses the pinhole camera model to determine depth using a priori knowledge size of the car and measurement of the car in image space. The static image model estimates range by using the ratio of the vehicle size and vehicle distance from optical axis but requires a priori knowledge of the size to estimate distance. The space geometry improves upon the static image technique by incorporating projective geometry to generate two planes defined by the vehicle shadow and camera pitch. The space geometry uses linear projection and inverse projection to estimate the position of the camera relative to the vehicle in front. The experimental setup was completed using limited field testing by using a single run of data for distances between 16 and 60 meters. An INS was not used to estimate the pitch of the camera. The process of measuring the car in image space is omitted from the manuscript. Capturing data using moving camera affixed to the car was missing, which would more accurately capture the real-world application.

Although literature is replete with monocular sensing techniques, standards do not exist for benchmarking the performance of a detect and avoid system. Self-assured well-clear definitions for sUAS are an active area of investigation as guidelines have yet to have been adopted by aviation authority. The Radio Technical Commission for

Aeronautics (RTCA) is a private organization that has advised aviation performance standards through a public-private partnership. The Special Committee 228 (SC228) of RTCA is targeting a release for January 2021 for Minimum Operational Performance Standards (MOPS) or electro-optical and infrared sensors for UAS [9].

The risk of a collision is a guiding safety metric for developing well-clear definitions, and may be estimated by dividing the probability of a Near Mid Air Collision (NMAC) using an avoidance maneuver by the probability of NMAC without an avoidance maneuver [10]. Members of the NASA project, UAS in the NAS, performed a simulation of the Detect and AvoID Alerting Logic for Unmanned Systems (DAIDALUS) [11] that illustrates an unresolved NMAC risk ratio of 0.05 for ~ 2 nautical miles [12] as shown in Figure 1, which is planned for inclusion in SC 228 MOPS in January 2021. The risk ratio captures the benefit of avoidance system for avoiding an NMAC. The risk ratio of 0.05 indicates that DAIDALUS prevents NMAC for 95% of the encounters when the intruder aircraft is detected at 2 NM.

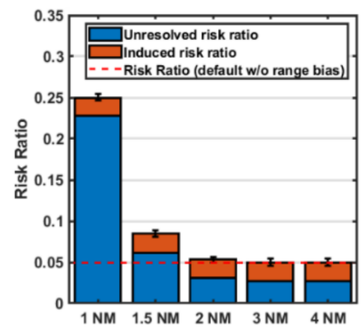

Figure 1: Risk Ratios variable Detection Range in Nautical Miles (NM) [12].

The FAA Center of Excellence for UAS Research funded an effort to develop DAA BVLOS requirements and the findings include recommendations for performance metrics for onboard sensors [13]. The proposed onboard sensor performance metrics include: Horizontal Range, Vertical Range, Horizontal Resolution, Vertical Resolution, Update Rate, Field of View, Sensor Latency, Sensitivity, Aircraft Classification, Probability of Detection, False Alarm Rate, Size, Weight, Power, and Reliability. Each of these metrics is scored 1 to 5 to indicate a capability level. For instance, a score of 4 for horizontal range indicates that the onboard sensor can resolve an object at 3.25 km and can maintain a horizontal well-clear definition of 2000 feet assuming the intruder aircraft speed is 50 m/sec and the sUAS is moving at 10 m/sec. A score of 4 for Field of View (FOV) has a horizontal FOV of 200 and 135 vertical FOV, which is equivalent to the viewing frustrum and range performance of a human pilot.

A literature search did not return any work on monocular camera ranging from sUAS and onboard vision based Detect and Avoid (DAA) would benefit from being able to range the intruder aircraft for avoidance planning. This work estimates intruder aircraft range using monocular camera using video collected in flight from a multirotor sUAS ownship of a fixed-wing sUAS and a GA plane. The model is developed using the contrast of the signal (aircraft) relative to background via curve fitting. Results are analyzed using the MOPS RTCA and the FAA BVLOS performance metrics.

III.Range Performance Model

The benchmark adopted in this work was developed in **[14]** to assess the range performance of an electro-optical detect and avoid system. The initial detection range, $\boldsymbol{R_0}$, as derived below, is integrated into a broader detection range inequality framework established in **[15]**. The metric of interest is target contrast against a background, as both visual detectability and computer vision filtering techniques rely on sufficient contrast to extract a foreground target from the local background. The metric of interest under consideration here is the Contrast to Noise Ratio (CNR) (Eq. 1),

$$\boldsymbol{CNR} = \frac{|\boldsymbol{I_S} - \boldsymbol{I_B}|}{\boldsymbol{I_N}}, \tag{1}$$

where $\boldsymbol{I_S}$ is signal intensity, $\boldsymbol{I_B}$ is the background intensity, and $\boldsymbol{I_N}$ is the noise intensity, measured in units of digital number. The intensity of intruder aircraft is $\boldsymbol{I_S}$, whereas $\boldsymbol{I_B}$ denotes the local background, which may be clouds, sky, or terrain. $\boldsymbol{I_N}$ is the local noise generated by photons scattering in the atmosphere and internal components of the sensors [16]. In outdoor scenes, $\boldsymbol{I_N}$ is typically dominated by shot noise. An ideal background intensity is a flat line because that the imaging of the background retains intensity and color constancy. An ideal signal curve will start at the background level and decrease as the target moves closer. The signal curve will have variations due to sporadic specular reflections (scintillations) of the aircraft. The ideal CNR curve would be influenced solely by the signal of the aircraft because the background remains static while the intruder aircraft grows within the imagery as it approaches the ownship. A CNR curve as a function of range can be extracted from a sequence of images captured in a single sortie. As per prior work [3], CNR may be empirically fitted to an exponential decay function of range, as atmospheric extinction is the dominant effect at long ranges (Eq. 2).

$$\boldsymbol{f_{CNR}(R) = ae^{-bR}}, \tag{2}$$

where $\boldsymbol{a}$ is a scaling factor, $\boldsymbol{b}$ is the rate of exponential decay, and $\boldsymbol{R}$ is range. Equation 2 may be rearranged to solve for the initial detection range, $\boldsymbol{R_0}$, as per Eq. 3. Note that $\boldsymbol{R_0}$ is an experimental metric that incorporates the dynamic sUAS environment and vision system hardware within the estimate.

$$\boldsymbol{R_0 = \frac{\ln a}{b} - \frac{\ln S_{th}}{b}}. \tag{3}$$

The maximum detection range, $\boldsymbol{R_0}$, is defined as the point along the curve where CNR exceeds a predefined threshold, $\boldsymbol{S_{th}}$. The value of the predefined threshold $\boldsymbol{S_{th}}$, was set to $\boldsymbol{S_{th}}$, = 4, as per prior work. This value is considered to be conservative given that results in **[14]** indicated that a human eye has a 90% probability of detecting an object with a minimum contrast ratio of 2.

Similarly, the precision in R_0 is derived from the calculus of errors (Eq. 4),

$$\boldsymbol{\delta R_0 = \sqrt{\left(\frac{\delta a}{ab}\right)^2 + \left[\frac{\delta b}{b^2}(\ln S_{th} - \ln\ a)\right]^2} + \delta R_{sys}}. \tag{4}$$

where $\boldsymbol{R_{sys}}$ is a systematic error in $\boldsymbol{R_0}$.

IV. Experimental Methodology

This section describes the aircraft, flight trajectories, and the available data. The data in this work is a subset of the data described in [4] and [17]. The ownship is the multirotor, ISAAC [18]: ICAROUS Sense and Avoid Characterization, where ICAROUS is Independent Configurable Architecture for Reliable Operations of Unmanned Systems [19]. The two-intruder aircraft are the Tempest (fixed-wing sUAS) and SR22 (GA) shown in Table 1. The machine vision system consisted of a Sony Action camera FDR-X1000Vwith a 41 Field of View lens was mounted to ISAAC using a gimbal that was programmed to be horizontally stabilized. The camera system operated at a data rate of 30 Hz at full-frame resolution, although ground truth collection was restricted to 15 Hz i.e. every other frame. Despite using a gimbal mount, camera pitching did occur during forward movement of the ownship.

Table 1: Aircraft.

Aircraft	Type	Image	Dimensions w x l x h (m)	Manufacturer
ISAAC (ownship)	sUAS multirotor		1 x 1 x 0.3	DJI
Tempest (intruder)	fixed wing sUAS		3.2 x 1 x 0.3	UASUSA
SR22 (intruder)	GA		11.68 x 7.92 x 2.72	Cirrus

The video for this work were collected at Beaverdam Airpark in Elberon, Virginia in 2018. ISAAC and the Tempest flew pre-programmed trajectories with safety pilots monitoring operations for both ownship and intruder sUAS, while the SR22 was flown manually for all sorties. Table 2 details the description of the dataset. An altitude separation of 30 meters was maintained between the ISAAC and the Tempest, while the ISAAC and the SR22 maintained a vertical separation of 180 meters for safety. The SR22 decreased altitude from the Initial Intruder Altitude to the Stable Intruder Altitude in the beginning part of sortie 4-6 in preparation for the head-on collision geometries with only the vertical separation.

Table 2: Dataset.

Date and time Takeoff (EST)	Sortie	Ownship	Ownship Altitude (m)	Intruder	Initial Intruder Altitude (m)	Stable Intruder Altitude (m)	Weather
2018/10/25 09:40 AM	1	ISAAC	200	Tempest	230	230	Partly Cloudy
	2	ISAAC	200	Tempest	230	230	Partly Cloudy
	3	ISAAC	200	Tempest	230	230	Partly Cloudy
2018/10/30 12:41	4	ISAAC	200	SR22	400	370	Sunny
	5	ISAAC	200	SR22	390	370	Sunny
	6	ISAAC	200	SR22	420	370	Sunny

Sorties 1 through 3 were recorded on the same day and captures the Tempest in partly cloudy conditions. The intruder aircraft is the SR22 for Sorties 4 through 6 in sunny conditions. Sample flight trajectories are shown in Figure 2 for multirotor (yellow) vs fixed-wing sUAS (red) and Figure 3 multirotor (yellow) vs GA (red). The Tempest was programmed to fly a rectangular flight pattern that was highly repeatable across Sorties 1-3 while ISAAC flew back and forth between two waypoints. The ICAROUS avoidance system activated once for ISAAC in Figure 2 shown by the southerly track, however, video from this part of the flight was not used for monocular ranging analysis **[19]**. However, the ownship paused at both the beginning and end of the waypoint pattern with intruder continuing on its collision course while collecting video.

Figure 2: Sample flight trajectories for Tempest (red) and ISAAC (yellow). Sorties 1 through 3.

The SR22 was manually flown using ground references to align for heading as shown in Figure 3. ISAAC flew the same two waypoint pattern from Sorties 1 through 3 for this GA vs multirotor encounters. Also shown in Figure 3 are two activations of ICAROUS heading North that were not included in monocular ranging analysis.

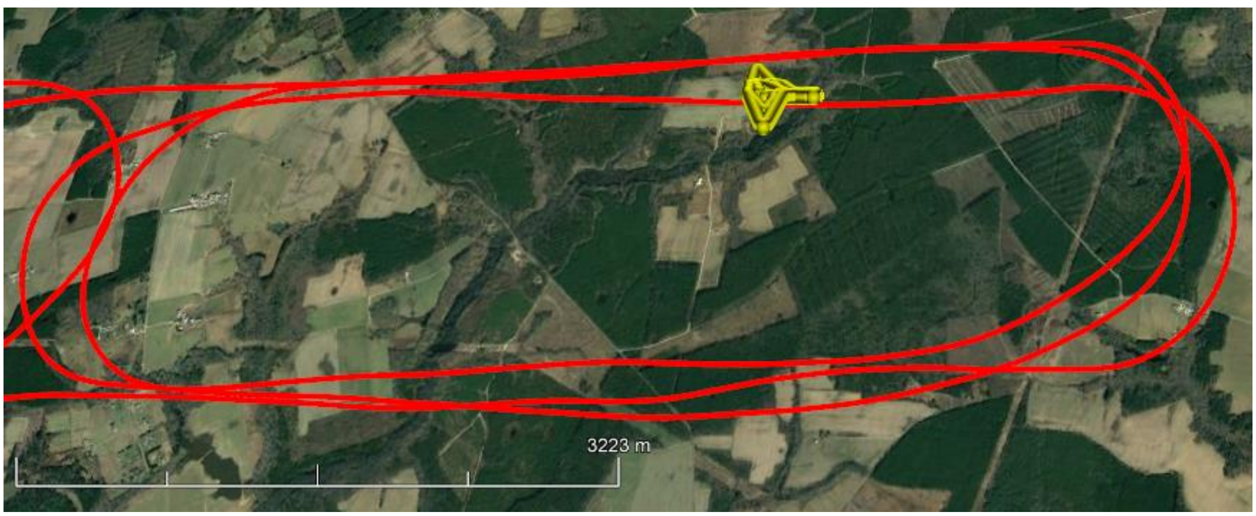

Figure 3: Sample flight trajectory for SR22 (red) and ISAAC (yellow). Sortie 4 through 6.

CNR values are experimentally computed from captured in-flight imagery of intruders on a head-on collision course with the ownship. The target location per-frame is manually extracted using segmented Ground Truth (GT) labels. The signal is computed as the highest outlier from the mean intensity from the 200 by 200 pixel Region of Interest (ROI) circumscribing the target. The local noise values are extracted from the 200 by 200 ROI. Initially, the background was computed using the 200 by 200 pixel ROI, however, computing a per-frame average of background intensity by segmenting the entire sky region as described in [4] improved the stability of the background intensity line.

V. Analysis and Results

This section presents results and analysis for the signal and background intensities followed by a discussion of the CNR curves for both intruder aircraft.

A. Signal and Background Intensities

The model for CNR presented in Section III is predicated upon atmospheric extinction being the dominant transfer function modulating the signal during its passage through the atmosphere. Other transfer functions tied to the ownship platform, optics and detector array are typically removed through a detailed calibration process. For the present experiments, the camera system was uncalibrated. In particular, the action camera utilized autoexposure to adjust sensor gain and shutter speed based on the average scene illumination. In this work, the two primary elements in the FOV are the sky and foliage, where the foliage possesses reduced reflectivity, and as such, is darker compared to the sky background. As the camera pitches downwards due to the forward motion of the ownship, the terrain with trees occupies a greater portion of the imagery. When the camera pitches downward and captures more of terrain in the imagery, the terrain brightens along with the sky because of the exposure correction. The number of pixels in the sky portion of the image is shown as function of distance with the black points in Figure 4 using the scale on the right side of the figure. The signal intensity, i.e. the aircraft, is shown by the blue points and the background intensity of the 200by 200 ROI is shown by the red points. Additionally, the region above the horizon is extracted as described in [4] and an per-frame average background intensity is computed and shown by the green points. Of note, the exposure correction impacts the 200 by 200 ROI background along with the per-frame average background intensity.

Due to the exposure correction, the analysis in this work is primarily restricted to a single forward motion of the sUAS bounded by pitching motions. The Appendix contains all sorties with their complete signals, average 200 by 200 ROI background intensity, the per-frame average background image, number of pixels above the horizon, and the corresponding CNR calculation.

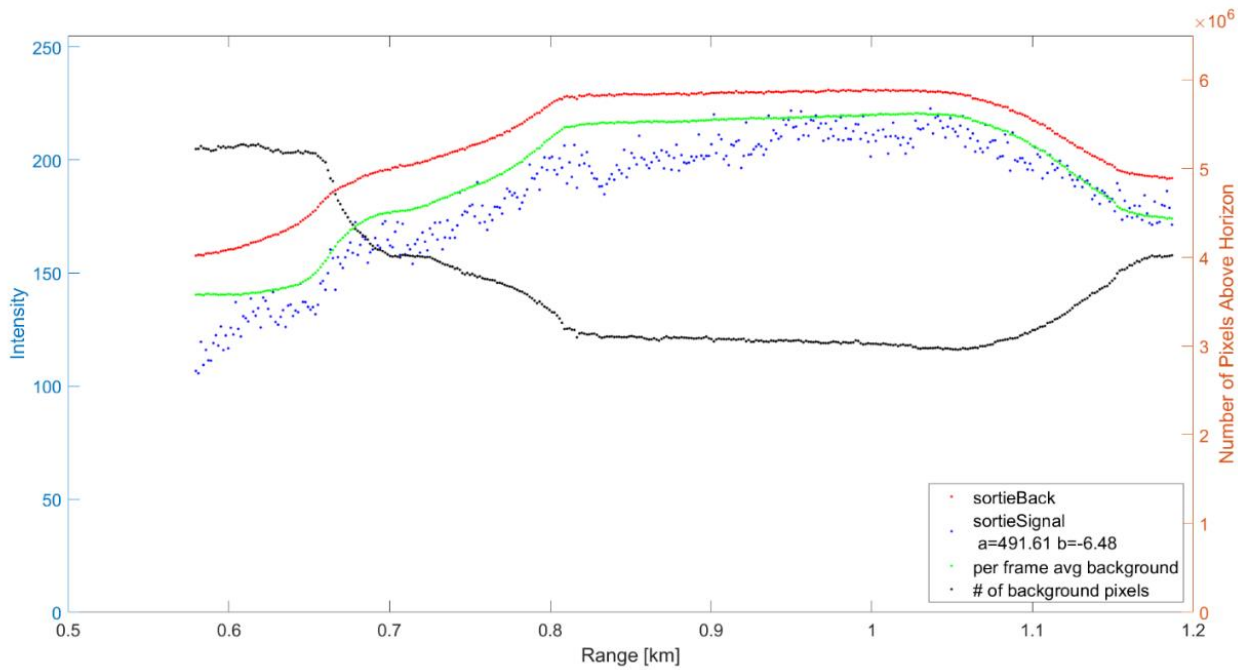

Figure 4: Sortie 1 Signal and Background Intensities

B. Empirical CNR

Figure 5 depicts the CNR as a function of range for all sorties. Each point represents a CNR value extracted from a single image. The results indicate the expected trend of increasing CNR with decreasing range. Oscillations in the raw CNR values may reflect scintillation, rolling shutter effects, dramatic changes in the local background due to an imprecise head-on geometry, and/or other temporal artifacts.

Tempest sorties 1 and 2 have CNR values bounded between 0 and 6 for the ranges between ~1.1 and 0.9 km. The CNR curve approximately varies 0.5 to 3 for sortie 1 while sortie 2 CNR varies 1 to 4.5. The similar results speak to robustness and repeatability of the CNR analysis for sortie 1 and 2 using limited data of ~200 meters of change in separation between the ownship and Tempest. CNR analysis for Tempest sortie 3 benefits from a longer aircraft closing encounter of 500 meters without variable pitching by the ownship (see Figure 7 in the Appendix for complete signal and background curves). Sortie 3 shows the expected CNR curve where the CNR increases substantially at closer ranges in response to lower aircraft signal.

The CNR value for SR22 sorties 4 through 6 is bounded between 0 and 30 for the bounds 2.5 to 0.8 km. The curve fit parameters for sorties 4 and 6 are similar. Careful replay of the sortie 6 reveals scintillations of the SR22 for distances greater than 2.4km, where the aircraft visually appears to sparkle along with greater variance in intensity. Sortie 5 also exhibits scintillations between 1.9 and 2.3 km and rolling shutter effects that dynamically affect the size of the target. The scintillations in sorties 4 and 6 correspond to the initial altitude decrease shown in Table 2.

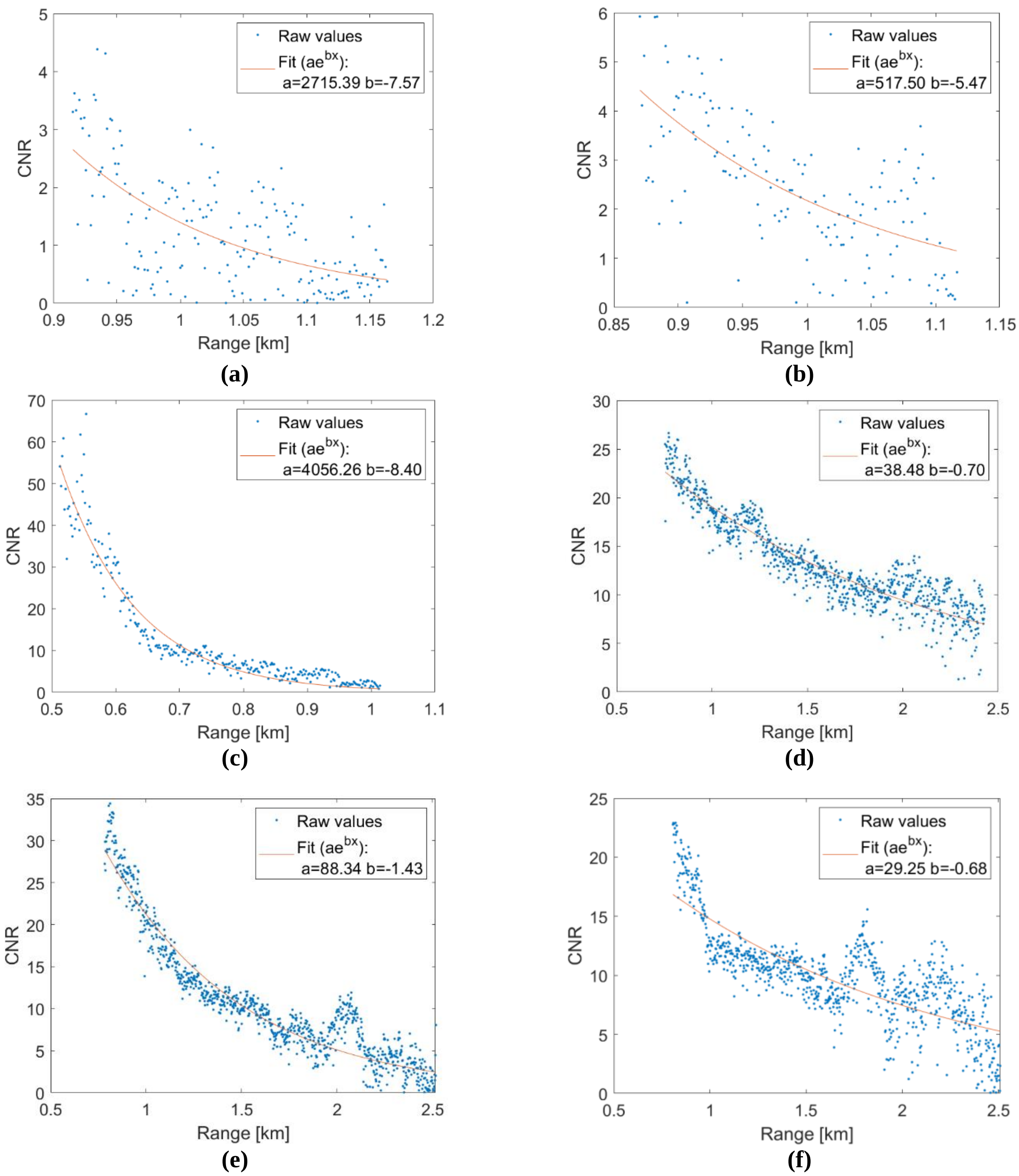

Figure 5:CNR as of function of Range: (a) Sortie 1 (Tempest Intruder), (b) Sortie 2 (Tempest Intruder), (c) Sortie 3 (Tempest Intruder), (d) Sortie 4 (SR22 Intruder), (e) Sortie 5 (SR22 Intruder), and (f) Sortie 6. (SR22 Intruder).

For each plot, an exponential curve as per Eq. 2 is fitted to the raw data, with fit values captured in the legend. Then, the $\boldsymbol{R_0}$ value is computed from the derived fit parameters and their associated error as per Eqs. 3 and 4 respectively. The results in Figure 5 show that is feasible to extract ranging of fixed-wing sUAS and GA using CNR curve fitting with this sensor, however, there is instability in the curve fitting parameters and more data is needed to robustly characterize the sensor. The initial detection ranges and associated error are shown in Table 3.

Table 3: Initial Detection and Associated Error.

Aircraft	Sortie	$\boldsymbol{R_0}$ [km]	$\boldsymbol{\Delta R_0}$ [km]
Tempest Multi-rotor sUAS	1	0.861	0.148
	2	0.889	0.144
	3	0.891	0.076
	Weighted Mean	**0.881**	**0.061**
SR 22 Fixed-wing GA Aircraft	4	3.23	0.068
	5	2.17	0.050
	6	2.92	0.105
	Weighted Mean	**2.763**	**0.037**

It is observed that $\boldsymbol{R_0}$ values of ~2.8 km for a fixed wing GA aircraft and ~0.9 km for fixed-wing sUAS are achievable with the current camera configuration. This GA result is about 1km from the 3.7 km (2 nm) MOPS for GA intruders [12] in support of SC228 and would receive a score of 3 out 5 for horizontal ranging described in [13]**,** where the minimum horizontal range is 1.22 km for a score of 3 and 3.25 km is the minimum horizontal range for a score of 4. The consistency of results for a given aircraft show the robustness of the methodology. The standard error of the weighted mean for $\boldsymbol{R_0}$ is 0.061 km for the Tempest sorties in partly cloudy conditions and within 0.037 km for the SR22. The discrepancy in the $\boldsymbol{R_0}$ SR22 results can be explained due to scintillations. The results were degraded by rolling shutter motion blurring that is apparent in the imagery. The $\boldsymbol{\Delta R_0}$ values indicate that curve parameters fit the CNR and range data well. The $\boldsymbol{\Delta R_0}$ were just under 0.15 km for sorties 1 and 2 that used approximately 0.2 km. The $\boldsymbol{\Delta R_0}$ were 0.05 to 0.1 km for sorties 3 through 6, which used ranges of greater than 0.5 km.

VI. Conclusion

This paper provides an operational performance assessment of an onboard sUAS vision system for sUAS and GA intruder aircraft separation distance estimation above the horizon. Results indicate that it is feasible for the proposed vision system, based on a 4k action camera with a 41 FOV lens, to detect a typical GA aircraft at ~2.7 km and a fixed-wing sUAS at ~ 0.9 km. An understanding of sensor performance plays a key role in establishing expectations for an onboard vision system within the context of the sUAS payload limitation: size, weight, and power. Future work includes applying this approach to additional intruder aircraft on diverse backgrounds: trees, fields, blue-sky, partly cloudy, and atmospheric scattering to generate a more robust estimate of range. Future work also includes using a global shutter sensor that is not subject to rolling shutter artefacts will improve the ranging results.

VII. References

[1] H. Shakhatreh, A. Sawalmeh, A. Al-Fuqaha, Z. Dou, E. Almaita and I. Khalil, "Unmanned Aerial Vehicles (UAVs): A Survey on Civil Applications and Key Research Challenges," *IEEE Access,* vol. 7, pp. 48572-48634 , 2019.

[2] A. Saxena, S. Chung and A. Ng, "3-D Depth Reconstruction from a Single Still Image," *International Journal of Computer Vision*, vol. 76, pp. 53-69, 2008.

[3] C. Minwalla, K. Ellis, S. Jennings, P. Thomas and R. Hornsey, "Range performance evaluation from the flight tests of a passive electro-optical aircraft detection sensor for unmanned aircraft systems," *J. Unmanned Veh. Syst.,* p. 1–19, 2016.

[4] C. Dolph, L. Glaab, B. Allen, M. Consiglio and K. Iftekharuddin, "An Improved Far-Field Small Unmanned Aerial System Optical Detection Algorithm," in *Digital Avionic Systems Conference*, San Diego, 2019.

[5] Van, "Real-Time Dense Stereo for Intelligent Vehicles," *IEEE Transactions on Intelligent Transportation Systems,* vol. 7, no. 1, pp. 38-50, 2006.

[6] A. Howard, "Real-time stereo visual odometry for autonomous ground vehicles," in *IEEE/RSJ International Conference on Intelligent Robots and Systems*, Nice, 2008.

[7] J. Wang, F. Zou, M. Zhang and Y. Li, "A Monocular Ranging Algorithm for Detecting Illegal Vehicle Jumping," in *International Conference on Green Informatics*, Fuzhou, 2017.

[8] Y. C. Q. Qian, F. Yang, W. Qian and Z. Li, "Monocular ranging system based on space geometry," in *SPIE Optical Engineering + Applications,*, San Diego, 2019.

[9] RTCA, "Minimum Performance Standards for Unmanned Aircraft Systems," [Online]. Available: https://www.rtca.org/wp-content/uploads/2020/08/sc-228_tor_rev_10_approved_06-11-2020.pdf. [Accessed 12 Nov Nov.].

[10] C. Chen, B. Gill, M. Edwards, S. Smearcheck, T. Adami, S. Calhoun, G. Wu, A. Cone and S. Lee, "Defining Well Clear Separation for Unmanned Aircraft Systems Operating with Noncooperative Aircraft," in *AIAA Aviation*, Dallas, 2019.

[11] C. Munoz, A. Narkawicz, G. Hagen, J. Upchurch, A. Dutle and M. Consiglio, " DAIDALUS: Detect and Avoid Alerting Logic for Unmanned Systems," in *Proceedings of the 34th Digital Avionics Systems Conference* , Prague, 2015.

[12] C. Serres, B. Gill and G. Wu, "EOIR Safety and Operational," 18 Feb. 2020. [Online]. Available: https://ntrs.nasa.gov/api/citations/20200002097/downloads/20200002097.pdf. [Accessed 12 Nov. 2020].

[13] M. Askelson and H. Cathey, "Small UAS Detect and Avoid Requirements Necessary for Limited Beyond Visual Line of Sight (BVLOS) Operations," U.S. Department of Transportation, Federal Aviation Administration, Washington, DC , 2017.

[14] H. Blackwell, "Contrast Thresholds of the Human Eye," *Journal of the Optical Society of America,* vol. 36, no. 11, pp. 624-643, 1946.

[15] C. Minwalla and K. Ellis, "Experimental Evaluation of PICAS: An Electro-Optical Array for Non-Cooperative Collision Sensing on Unmanned Aircraft Systems," in *AIAA SciTech*, Grapevine,Tx, 2017.

[16] G. Holst, Electro-Optical Imaging System Performance, Winterpark: JCD Publishing and SPIE, 2017.

[17] B. Duffy, S. Balachandran, M. Consiglio, L. Glaab, C. Munoz and e. al, "Sense and Avoid Characterization of the ICAROUS Architecture," National Aeronautics and Space Administration, Hampton, Virginia, 2020.

[18] M. Consiglio, L. Glaab and C. Munoz, "Sense and Avoid Characterization of the Independent Configurable Architecture for Reliable Operations of Unmanned Systems," in *Air Traffic Management Research* , Vienna, Austria, 2019.

[19] S. Balachandran, C. Munoz, M. Consiglio, M. Feliu and A. Patel, "Independent Configurable Architecture for Reliable Operation of Unmanned Systems with Distributed Onboard Services," in *38 IEEE/AIAA 37th Digital Avionics Systems Conference* , London, UK, 2018.

VIII. Appendix

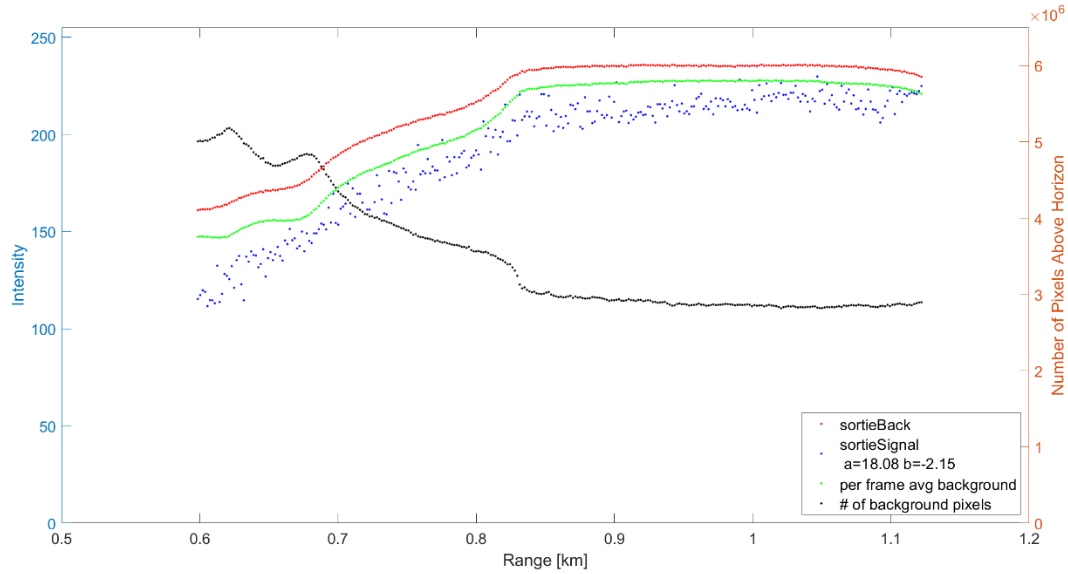

Figure 6: Sortie 2 Signal and Background Intensities

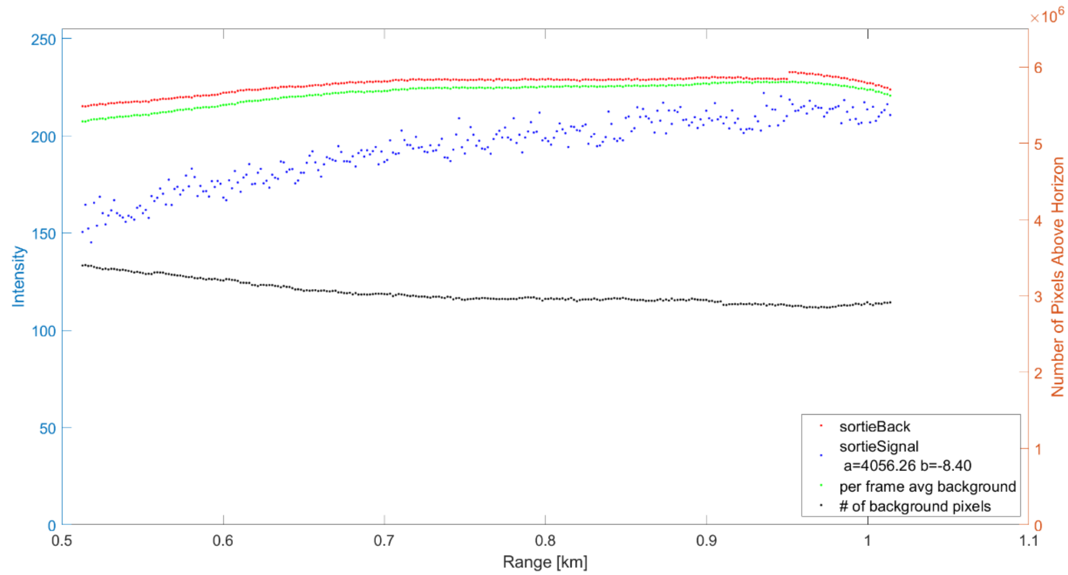

Figure 7: Sortie 3 Signal and Background Intensities

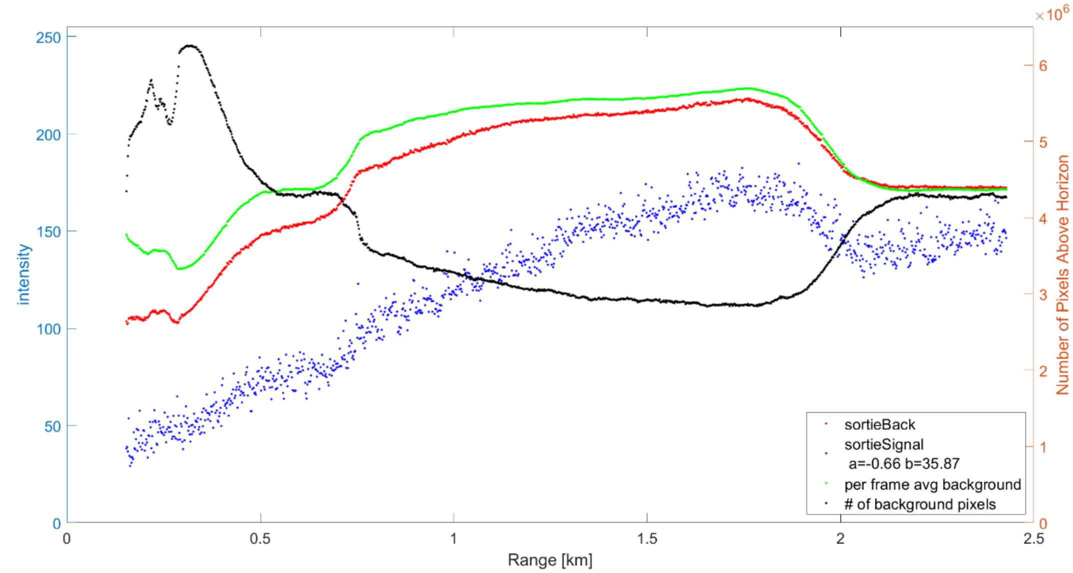

Figure 8: Sortie 4 Background and Signal Intensities

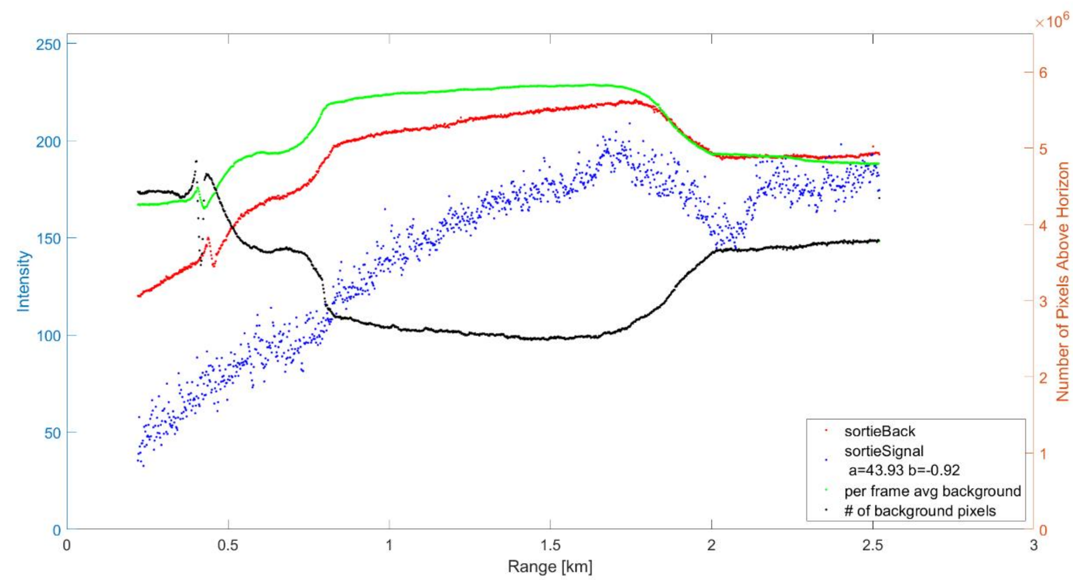

Figure 9: Sortie 5 Background and Signal Intensities

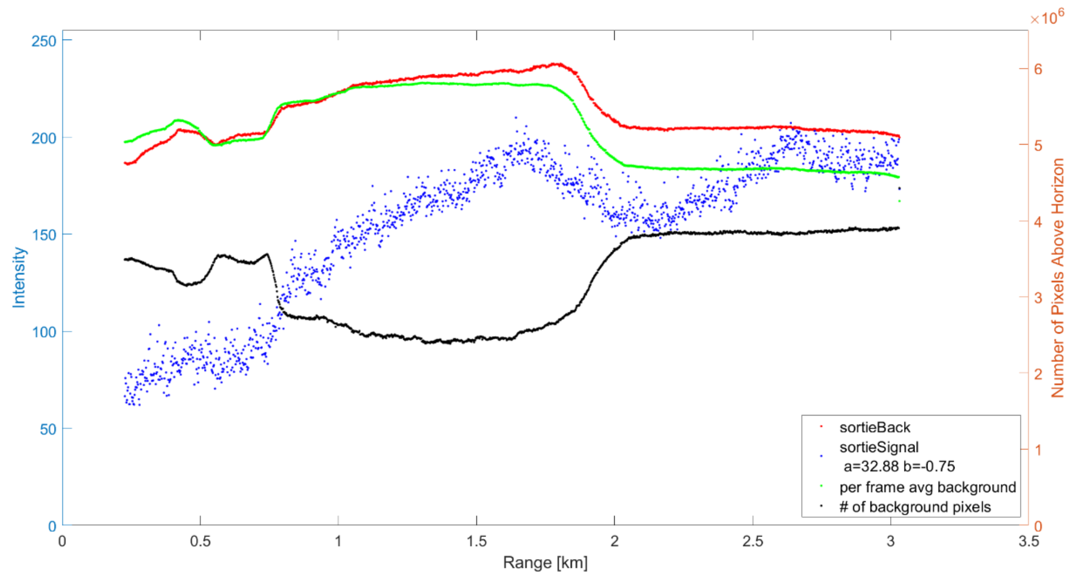

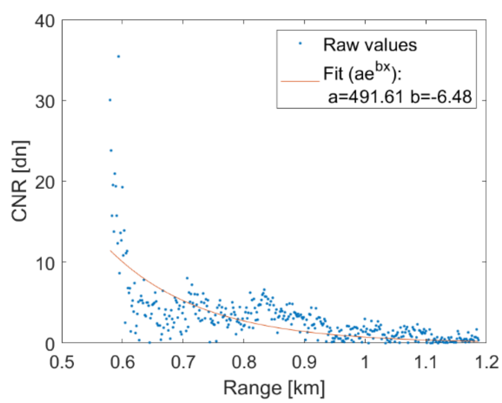

Sortie 1

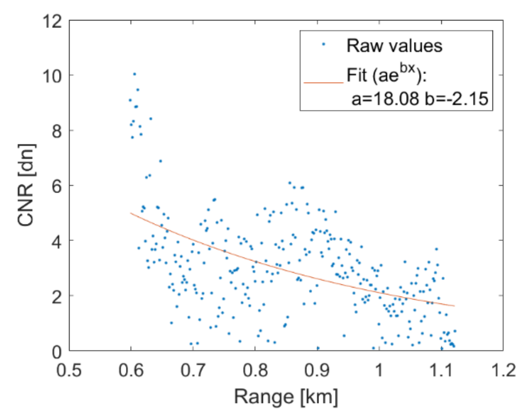

Sortie 2

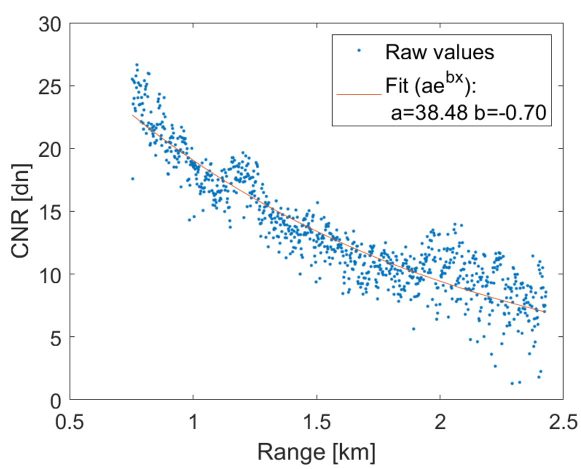

Sortie 4

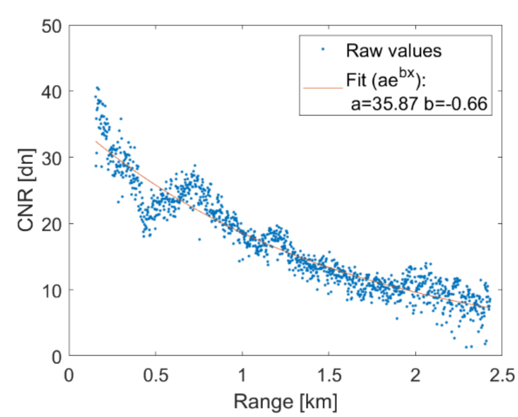

Sortie 5

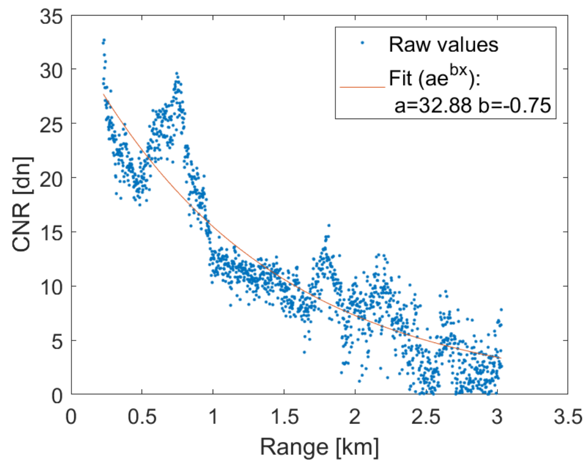

Sortie 6

Figure 10: Complete CNR Curves